

# **IEICE** **TRANSACTIONS**

## **on Communications**

DOI:10.23919/transcom.2024EBP3090

This advance publication article will be replaced by the finalized version after proofreading.

**A PUBLICATION OF THE COMMUNICATIONS SOCIETY**



The Institute of Electronics, Information and Communication Engineers  
Kikai-Shinko-Kaikan Bldg., 5-8, Shibakoen 3chome, Minato-ku, TOKYO, 105-0011 JAPAN

## PAPER

# Three-dimensional Complex Permittivity Reconstruction via Wave-number Space Based Deep Neural Network for Microwave Breast Imaging

Peixian ZHU<sup>†a)</sup>, Student Member and Shouhei KIDERA<sup>†b)</sup>, Senior Member

**SUMMARY** This study introduces a three-dimensional (3D) complex permittivity profile reconstruction using a deep neural network, where wave-number space data compression is applied to reduce the dimension of input data. Four-dimensional scattered data are converted into a 3D complex permittivity profile by integrating a 3D convolutional autoencoder and a multilayer perceptron. The reconstruction accuracy is further improved through efficient skin surface rejection preprocessing via a fractional derivative model. An experimental study, using simplified 3D breast phantom and an ultrawideband radar module shows that our proposed scheme provides accurate estimates for 3D reconstruction in terms of relative permittivity and conductivity.

**key words:** Microwave breast cancer detection, Deep neural network (DNN), Complex permittivity reconstruction, Ultrawideband (UWB) radar, Skin surface rejection (SSR).

## 1. Introduction

Breast cancer is the leading contributor to cancer-related fatalities among women in worldwide. In 2020, approximately 2.26 million cases were documented [1]. X-ray and ultrasound methods are the predominant modalities for mammography. Nonetheless, the X-ray approach poses a threat because it requires high-energy exposure to healthy cells and compression of the breasts during diagnosis, which causes patient discomfort. Moreover, ultrasound-based diagnosis demands considerable experience and skill for cancer discrimination, making the early detection of breast cancer challenging. In light of the significance of early detection and treatment for enhancing patient survival rates, microwave breast cancer imaging has emerged as a promising alternative. This method exhibits several advantages, including low costs, compactness, painlessness, and safety, which can promote the frequency of cancer screening. Furthermore, normal adipose and malignant tumor tissues show a significant dielectric contrast in the microwave frequency band [2, 3]. These findings propel the advancement of microwave mammography, offering a potential breakthrough for more effective breast cancer screening methods.

Although radar-based methods are commonly used as a primary imaging technique for microwave breast cancer detection, [4–7], it suffers a high false-positive rate, particularly

in dense breast tissues, due to the limited dielectric contrast between cancerous and fibroglandular tissue. The tomographic approach, also known as inverse scattering analysis, offers a distinctive advantage by enabling the quantitative estimation of the complex permittivity profile by solving domain integral equations [8–11]. Given the nonlinear, ill-posed nature of the problem, retaining accurate reconstruction profiles is difficult, especially for high-contrast breast media. This issue is distinct in three-dimensional (3D) models, where a substantial increase in the number of unknowns intensifies the computational complexity of the reconstruction process.

To address the aforementioned challenge, numerous researchers have performed optimization based on deep neural networks (DNNs) using microwave scattered data to retain accurate two-dimensional (2D) or 3D reconstruction profiles [12–14]. In a previous study [15], a comparative U-Net convolutional neural network was incorporated into the Born iterative method. However, the input data of U-Net in this method need to be computed initially through the Born iterative method, thus increasing the computational cost. In the study [16], while 3D reconstruction was obtained using five frequency samples by combining 2D contrast source inversion and U-Net, the 2D results of the inverse problem are needed, leading to high computational complexity. To achieve accurate 3D permittivity profile reconstruction within an acceptable timeframe, we previously introduced a direct conversion scheme from scattered data to simplified 3D profiles of complex permittivity; this method combines skin surface rejection (SSR) and a neural network scheme [17]. Conversely, as the number of unknowns substantially increases, reconstructing high-spatial-resolution 3D profiles, such as those with 1 mm voxel resolutions, becomes challenging.

In light of the above difficulty, this paper introduces a DNN scheme with dimension reduction for 3D reconstruction. This approach incorporates wave-number space (WS) data filtering and data compression based on a convolutional autoencoder (CAE). In this method, a 3D spatial profile for each training breast model is converted into a WS to reduce the unknowns using a low-pass filter (LPF). These WS data are further compressed using the 3D CAE, and the compressed output of the encoder is extracted. In this context, the trained encoder part of the CAE is replaced with a fully connected (FC) multilayer perceptron (MLP) to convert

<sup>†</sup>P. Zhu and S. Kidera are with Graduate School of Informatics and Engineering, The University of Electro-Communications, Tokyo, Japan.

a) E-mail: zhu.peixian@uec.ac.jp

b) E-mail: kidera@uec.ac.jp

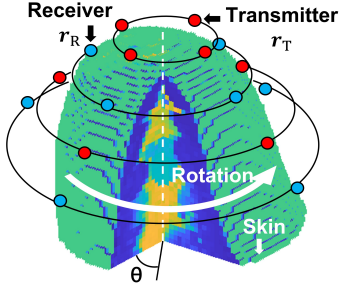


Fig. 1: Observation model. Array with multiple transmitters and receivers is rotated at external area of breast.

four-dimensional (4D) scattered data into a 3D complex permittivity profile. Notably, reflections from the skin surface are dominant in scattered 4D data and should be suppressed using an appropriate SSR scheme. These schemes also improve the effectiveness of learning in 3D CAE or FC MLP. Because these DNNs can train the differential components of a breast profile by eliminating common components, such as skin and adipose tissue. Thus, the main contributions of this study are as follows:

1. Significantly reducing the dimensions of input data via WS- or 3D-CAE-based compression enhances training efficiency, even when using a small number of training data.
2. The SSR scheme helps remove redundant components from scattered data and enables the extraction of differential parts of each profile.
3. The 4D scattered data can be directly converted into a 3D complex permittivity profile by the trained DNN; this does not require any optimization process, such as inverse scattering analysis.

Experimental validation using an ultrawideband (UWB) radar module and a simplified quantitative breast phantom demonstrates that our proposed scheme successfully reconstructs 3D complex permittivity profiles.

## 2. Method

### 2.1 Observation Model

Fig. 1 shows the observation model in this study. Transmitters and receivers are configured into circular arrays that rotate along the vertical direction.  $s(t, \mathbf{r}_T, \mathbf{r}_R, \theta)$  denotes the scattered electric field from a source position  $\mathbf{r}_T$  to an observation position  $\mathbf{r}_R$  at the rotation angle  $\theta$ , where  $t$  is time.

### 2.2 Skin Surface Rejection Process

The main idea of this study is directly converting multidimensional scattered data into a 3D complex permittivity profile via a DNN scheme. For DNN preprocessing, we introduce efficient clutter suppression for skin reflection, which is strong and may mask the internal response.

In our previous studies [17, 18], we proposed an efficient SSR scheme based on a fractional derivative (FD) model, hereinafter called SSR-FD, to eliminate the effect of skin surface reflections and improve the accuracy of reconstruction [17]. Here, we briefly introduce the SSR-FD method as follows. First, the reference signal of SSR-FD schemes  $s^{\text{ref}}(t, \mathbf{r}_T, \mathbf{r}_R, \theta)$  is provided by calculating the following:

$$\bar{s}^{\text{ref}}(t, \mathbf{r}_T, \mathbf{r}_R) = \frac{1}{N_\theta} \sum_{i=1}^{N_\theta} s^{\text{ref}}(t, \mathbf{r}_T, \mathbf{r}_R, \theta_i) \quad (1)$$

where  $\theta_i$  denotes the  $i$ -th rotation angle and  $N_\theta$  is the total number of sampled rotation angles. If the distance between the skin and the elements is constant during array rotation, then the averaging operation in Eq. (1) will enhance the signal-to-noise ratio, which is useful for postsuppression.

A past study [17] demonstrated that the SSR-FD could compensate for frequency-dependent scattering effects, which are mainly caused by the mutual coupling between the skin and antenna or other near-field effects. In this method, the skin surface response is expressed as the following FD model:

$$\tilde{s}_{\text{ref}}(t, \mathbf{r}_T, \mathbf{r}_R; \alpha) = \mathcal{F}^{-1}[(j\omega)^\alpha \bar{s}^{\text{ref}}(\omega, \mathbf{r}_T, \mathbf{r}_R)] \quad (2)$$

where  $\bar{s}^{\text{ref}}(\omega, \mathbf{r}_T, \mathbf{r}_R) = \mathcal{F}[\bar{s}^{\text{ref}}(t, \mathbf{r}_T, \mathbf{r}_R)]$ , and  $\mathcal{F}$  denotes the Fourier transform,  $(j\omega)^\alpha$  denotes the FD operator using an additional parameter  $\alpha$ . Then, the clutter-eliminated signal produced by the SSR-FD as  $\tilde{s}_{\text{FD}}(t, \mathbf{r}_T, \mathbf{r}_R, \theta)$  is formed as follows:

$$\tilde{s}_{\text{FD}}(t, \mathbf{r}_T, \mathbf{r}_R, \theta) = s(t, \mathbf{r}_T, \mathbf{r}_R, \theta) - \hat{A} \tilde{s}^{\text{ref}}(t - \hat{\tau}, \mathbf{r}_T, \mathbf{r}_R; \hat{\alpha}) \quad (3)$$

where  $\hat{A}$ ,  $\hat{\tau}$ , and  $\hat{\alpha}$  are optimized as follows:

$$(\hat{A}, \hat{\tau}, \hat{\alpha}) = \underset{A, \tau, \alpha}{\operatorname{argmin}} \int_{T_r}^{T_r+T_w} |s(t, \mathbf{r}_T, \mathbf{r}_R, \theta) - \hat{A} \tilde{s}^{\text{ref}}(t - \hat{\tau}, \mathbf{r}_T, \mathbf{r}_R; \hat{\alpha})|^2 dt \quad (4)$$

where  $T_r$  represents the rise time of  $s(t, \mathbf{r}_T, \mathbf{r}_R, \theta)$  and  $T_w$  denotes the temporal window length.

### 2.3 Dimension Reduction by Wave-number Space Expression

Reducing the dimensions of input data is an essential part of DNN design for obtaining high-spatial-resolution 3D profiles via DNN scheme. In this study, we introduce two types of schemes for dimension reduction. The first one is based on Fourier-basis expression: WS conversion is applied to the 3D complex permittivity profile to reduce the WS data dimension. The second one is CAE-based dimension reduction, which is described in the next subsection.

WS data compression is described as follows. We define a discrete 3D profile for relative permittivity  $\epsilon_r$  and conductivity  $\sigma$  as  $i_\epsilon(x_i, y_j, z_k)$  and  $i_\sigma(x_i, y_j, z_k)$ , respectively,

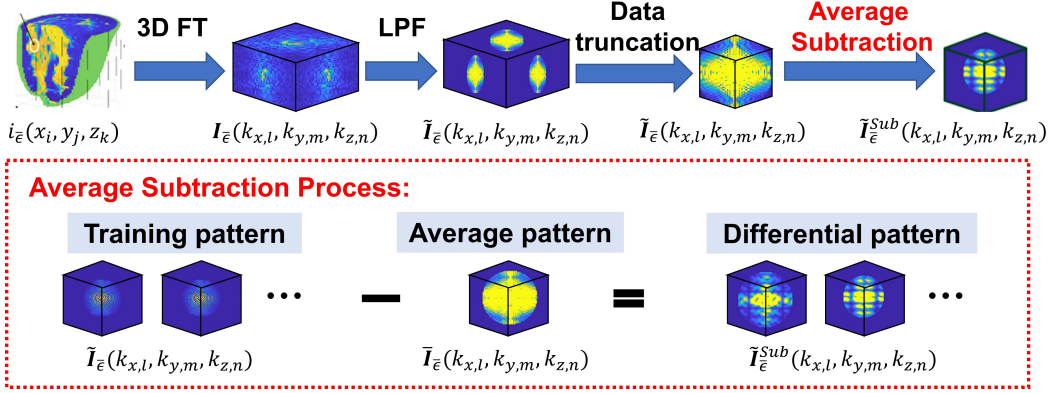


Fig. 2: Schematic illustration of the dimension reduction of 3-D breast profile in the proposed approach.

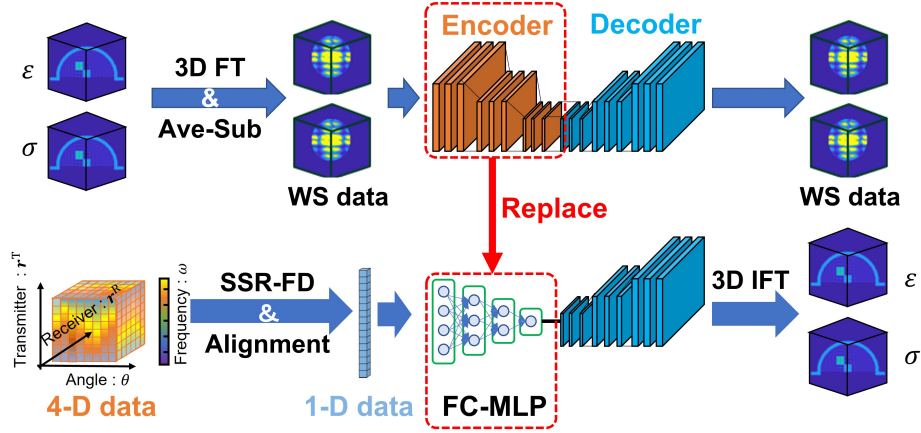


Fig. 3: Processing flow of the proposed scheme. First step: WS compressed data via Ave-sub and SSR-FD processes are input to 3D CAE model. Second step: Encoder part of 3D-CAE is replaced by FC-MLP to convert the 4-D scattered data to spatial frequency data of complex permittivity profile for relative permittivity ( $\epsilon$ ) and conductivity ( $\sigma$ )

where the subscripts  $i$ ,  $j$ , and  $k$  denote the voxel indexes along the  $x$ ,  $y$ , and  $z$  directions, respectively. These parameters can be converted into complex permittivity at a specific angular frequency  $\omega$  as follows:

$$i_{\bar{\epsilon}}(x_i, y_j, z_k) = i_{\epsilon}(x_i, y_j, z_k) - i \frac{i_{\sigma}(x_i, y_j, z_k)}{\epsilon_0 \omega} \quad (5)$$

Here,  $\epsilon_0$  denotes the permittivity of free space. Then, the above 3D complex permittivity profile is converted in the WS as  $I_{\bar{\epsilon}}(k_{x,l}, k_{y,m}, k_{z,n})$  using 3D Fourier transform, and the zero-frequency component is shifted to the center of spectrum. The following LPF is applied to reduce the dimension of  $I_{\bar{\epsilon}}(k_{x,l}, k_{y,m}, k_{z,n})$ :

$$\tilde{I}_{\bar{\epsilon}}(k_{x,l}, k_{y,m}, k_{z,n}) = \begin{cases} I_{\bar{\epsilon}}(k_{x,l}, k_{y,m}, k_{z,n}) & (K(k_{x,l}, k_{y,m}, k_{z,n}) \leq K_{\text{cutoff}}) \\ 0 & (\text{otherwise}) \end{cases} \quad (6)$$

where  $K(k_{x,l}, k_{y,m}, k_{z,n})$  denotes the distance from  $(k_{x,l}, k_{y,m}, k_{z,n})$  to the WS origin and  $K_{\text{cutoff}}$  is the cutoff wave number. The processing is also shown in Fig. 2. Here, the parameter  $K_{\text{cutoff}}$  is selected by considering the balance

between the spatial resolution of the reconstruction profile and the compression effect of data dimension. A high  $K_{\text{cutoff}}$  value leads to a low compression rate, resulting in a slow optimization convergence or over-fitting. In contrast, a low  $K_{\text{cutoff}}$  leads to a low spatial resolution, causing difficulties in detecting small cancer tissues.

To focus on differential patterns of wave-number data as  $\tilde{I}_{\bar{\epsilon}}(k_{x,l}, k_{y,m}, k_{z,n})$ , we remove common components of  $\bar{I}_{\bar{\epsilon}}(k_{x,l}, k_{y,m}, k_{z,n})$  as follows:

$$\tilde{I}_{\bar{\epsilon}}^{Sub}(k_{x,l}, k_{y,m}, k_{z,n}) = \tilde{I}_{\bar{\epsilon}}(k_{x,l}, k_{y,m}, k_{z,n}) - \bar{I}_{\bar{\epsilon}}(k_{x,l}, k_{y,m}, k_{z,n}) \quad (7)$$

where  $\bar{I}_{\bar{\epsilon}}(k_{x,l}, k_{y,m}, k_{z,n})$  denotes the average pattern of  $\tilde{I}_{\bar{\epsilon}}(k_{x,l}, k_{y,m}, k_{z,n})$  with  $n$  samples. We call this processing procedure average subtraction (Ave-Sub). This scheme is also shown in Fig. 2.

#### 2.4 Dimension Reduction by 3D-CAE

We introduce 3D-CAE-based data compression, to further reduce the dimension of the input data for the post DNN process. In this scheme, we reduce the data dimension by extracting a hidden layer of the 3D CAE, where the input and output data of the 3D CAE are defined as the filtered WS

data described in the Section 2.3. In particular, the feature data in the hidden layers, defined as  $\mathbf{z} \in \mathcal{R}^{N_h \times 1}$  are computed through supervised learning in the 3D CAE network, where the input and output data are defined as  $\tilde{I}_{\epsilon}^{\text{Sub}}(k_{x,l}, k_{y,m}, k_{z,n})$ . This CAE scheme helps reduce redundant dimensions or expressions in input data via nonlinear conversion; this is usually better than linear compression schemes, such as singular value decomposition. We call the proposed dimension reduction strategy as 3D-WS-CAE, which combines with the WS (described in Sec. 2.3) and the 3D CAE reduction schemes. After the training phase of the 3D CAE is completed, the input 3D data  $\tilde{I}_{\epsilon}^{\text{Sub}}(k_{x,l}, k_{y,m}, k_{z,n})$  are converted into the one-dimensional (1D) feature vector  $\mathbf{z}$ , which is processed in the post DNN phase, described in the following section. Figure 3 denotes the processing flow of the proposed method by introducing the 3D-CAE with WS compressed data. Compared to ordinary 3D-CAE downscaling, the proposed 3D-WS-CAE downscaling has the following benefits: Reducing a number of dimension to improve the computational efficiency, which also contributes a noise reduction.

## 2.5 SSR-FD-MLP integrating with 3D-FFT-CAE

In this study, an FC-MLP-based complex permittivity profile reconstruction scheme [17] is introduced to retain the full 3D image of breast media. Here, the SSR-FD-processed scattered data, denoted as  $S_{\text{FD}}(t, \mathbf{r}_T, \mathbf{r}_R, \theta)$ , are converted to frequency-domain data as  $S_{\text{FD}}(\omega, \mathbf{r}_T, \mathbf{r}_R, \theta)$  via 1D Fourier transform along  $t$ . These 4D scattered data are flatten to the following 1D input vector  $\mathbf{X}$ :

$$\mathbf{X} \equiv [\xi_{1,1,1,1}, \dots, \xi_{1,1,1,l}, \xi_{1,1,2,1}, \dots, \xi_{1,1,2,l}, \dots, \xi_{1,1,k,1}, \dots, \xi_{1,1,k,l}, \xi_{1,2,1,1}, \dots, \xi_{1,2,1,l}, \xi_{1,2,2,1}, \dots, \xi_{1,2,2,l}, \dots, \xi_{1,2,k,1}, \dots, \xi_{1,j,k,l}, \dots, \xi_{i,1,1,1}, \dots, \xi_{i,1,1,l}, \dots, \xi_{i,1,2,1}, \dots, \xi_{i,1,2,l}, \dots, \xi_{i,1,k,1}, \dots, \xi_{i,j,k,l}] \quad (8)$$

Here,  $\xi_{i,j,k,l}$  is defined as follows:

$$\xi_{i,j,k,l} \equiv S_{\text{FD}}(\omega_i, \mathbf{r}_{T,j}, \mathbf{r}_{R,k}, \theta_l) \quad (9)$$

where  $S_{\text{FD}}(\omega_i, \mathbf{r}_{T,j}, \mathbf{r}_{R,k}, \theta_l)$  denotes the scattered data at the  $i$ -th angular frequency from the  $j$ -th transmitter to the  $k$ -th receiver at  $l$ -th angle.

To connect the trained 3D CAE network, we convert the input vector  $\mathbf{X}$  into the feature vector  $\mathbf{z}$  (defined in Sec. 2.3) via a FC MLP, as shown in Fig. 3. After the training sequences of this FC MLP are completed, non-trained 4D scattered data are converted into 3D WS data as  $\tilde{I}_{\epsilon}^{\text{Sub}}(k_{x,l}, k_{y,m}, k_{z,n})$ . Then, the reconstructed complex permittivity profile  $\tilde{I}_{\epsilon}(x, y, z)$  is obtained as follows:

$$\begin{aligned} \tilde{I}_{\epsilon}(x, y, z) \\ = \mathcal{F}_{3\text{D}}^{-1} [\tilde{I}_{\epsilon}^{\text{Sub}}(k_{x,i}, k_{y,j}, k_{z,k}) + \bar{I}_{\epsilon}(k_{x,i}, k_{y,j}, k_{z,k})] \end{aligned} \quad (10)$$

where  $\mathcal{F}_{3\text{D}}^{-1}$  denotes the inverse 3D Fourier transform. The 3D WS data in the original size  $\tilde{I}_{\epsilon}^{\text{Sub}}(k_{x,l}, k_{y,m}, k_{z,n})$  and the average pattern in the original size  $\bar{I}_{\epsilon}(k_{x,l}, k_{y,m}, k_{z,n})$  are

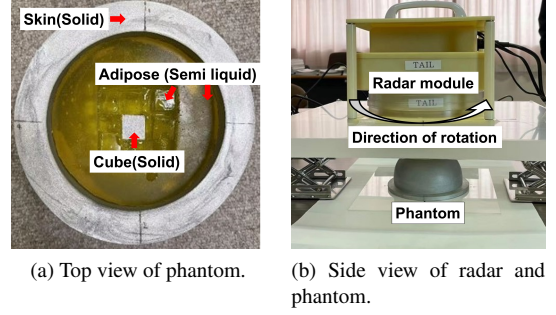


Fig. 4: Experimental setup for UWB radar and simplified breast phantom.

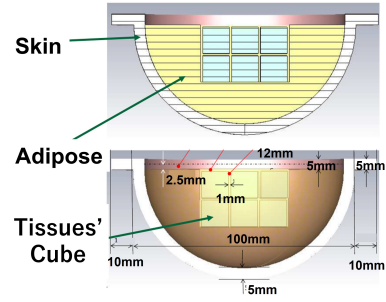


Fig. 5: 3-D structure of simplified breast phantom. Central 18 cubes are exchangeable in terms of adipose, fibroglandular, and cancer mimicking dielectric cells.

recovered by applying zero padding to  $\tilde{I}_{\epsilon}^{\text{Sub}}(k_{x,l}, k_{y,m}, k_{z,n})$  and  $\bar{I}_{\epsilon}(k_{x,l}, k_{y,m}, k_{z,n})$ , respectively.

## 3. Experimental Validation

### 3.1 Observation and Target Model

Experimental validation based on a simplified 3D breast phantom is conducted as follows. Fig. 4 shows the experimental setup, including a handheld UWB radar module, developed by Prof. T. Kikkawa at Hiroshima University [19]. This UWB module can be operated at frequencies of 3.1-10.0 GHz. The array, consisting of eight transmitters and eight receivers, is placed along the circumference of a hemisphere with a 75 mm radius. It can measure scattered data from different illumination angles within  $360^\circ$  with  $40^\circ$  intervals. For reliable quantitative error analysis, we introduce the 3D breast phantom in Fig. 5. The phantom is designed such that the skin and the surrounding adipose media are made by solid or semisolid materials. It includes 18 cubic cells (12 mm length) embedded in the center of the phantom. Table 1 provides the dielectric properties of 5 types of dielectric materials at 2.4 GHz, namely, adipose, fibroglandular, and three variations of cancer tissues, which have low, moderate, and high dielectric properties, respectively. By changing the cell combination patterns, we generate 66 patterns for the post DNN scheme.

Table 1: Dielectric parameter for each tissue cell.

Tissue (State)	Relative permittivity	Conductivity [S/m]
Adipose (semi-solid)	3.6	0.09
Skin	22.84	0.97
Mammary gland	22.84	0.97
Cancer type 1	27.51	1.07
Cancer type 2	46.63	2.04
Cancer type 3	32.05	1.56

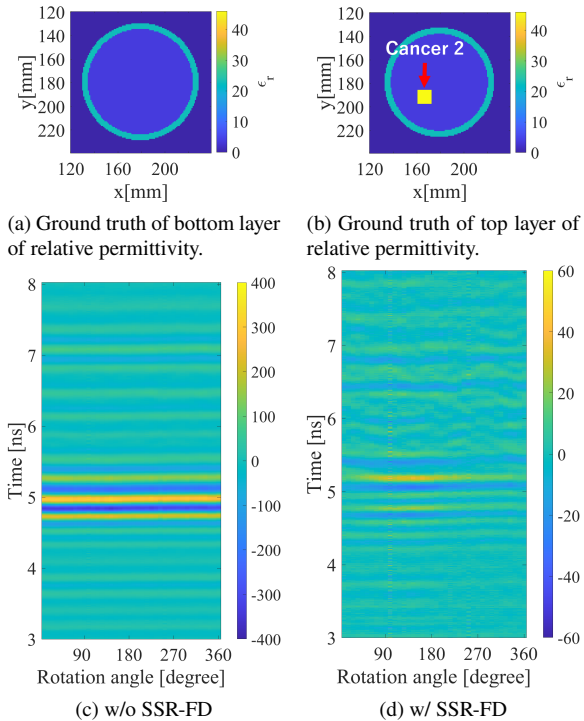


Fig. 6: Performance example 1 of the SSR-FD process.

### 3.2 Data and Results

#### 3.2.1 Performance of Skin Surface Rejection (SSR-FD)

The SSR-FD performance is described as follows. The reference signal, defined as  $s^{\text{ref}}(t, \mathbf{r}_T, \mathbf{r}_R, \theta_i)$  in Eq.(1), is measured when all 18 cells are allocated as adipose tissue to attain only the skin reflection component. Fig. 6 and Fig. 7 show 2 examples of SSR-FD application results. As shown these figures, the SSR-FD scheme effectively suppresses the strong skin reflection and can extract the response from inner region, namely, cancer or fibroglandular tissue. The color-bar scales in Figures 6 and 7 - (c) (w/o SSR-FD) are approximately 6.6 (400/60) times larger than those in Figures 6 and 7 - (d) (w/ SSR-FD). Focusing on the Figures 6 and 7 - (c) (w/o SSR-FD), strong reflection signals from the skin are observed in the range of 4.7 ns  $\leq t \leq 5.3$  ns with the maximum strength over 300. In contrast, as indicated in Figures 6 and 7 - (d) (w/ SSR-FD), these skin reflection signals are considerably suppressed by the SSR-FD scheme within the same temporal range, allowing for clearer reflections from the internal area (e.g., cancer or fibroglandular mimicked

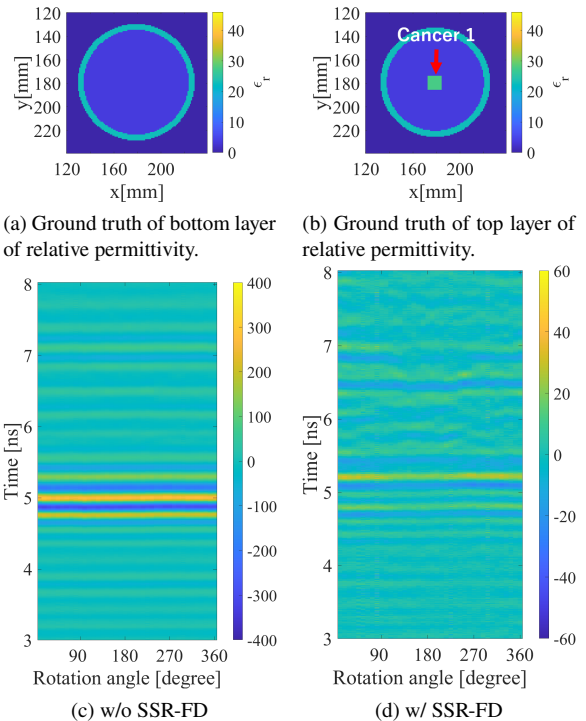


Fig. 7: Performance example 2 of the SSR-FD process.

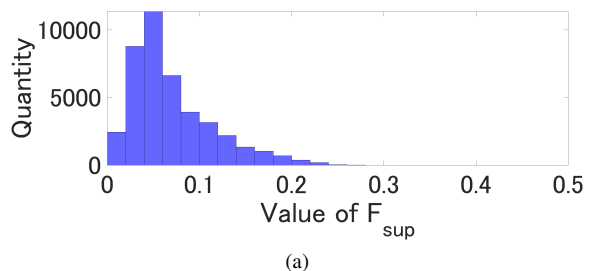


Fig. 8: Histogram of  $F_{\text{sup}}$  in SSR-FD process.

cells) at  $t \geq 5.3$  ns. Moreover, since the cancer location in Fig. 6-(b) is off-center, the signal strength and time delays in Fig. 6-(d) vary with the rotation angle. Conversely, in Fig. 7, where the cancer cell is positioned at the center of the breast, the signal strengths and delays remain relatively constant across different rotation angles. These results further demonstrate that our SSR-FD scheme effectively extracts responses from the internal area by suppressing skin reflection signals.

For the quantitative evaluation of the suppression performance of SSR-FD, the following criteria are defined:

$$F_{\text{sup}} = \frac{\max_{T_r < t < T_r + W} \tilde{s}_{\text{wSSR}}(t)}{\max_{T_r < t < T_r + W} \tilde{s}_{\text{woSSR}}(t)} \quad (11)$$

where  $\tilde{s}_{\text{woSSR}}(t)$  and  $\tilde{s}_{\text{wSSR}}(t)$  denote the scattered responses without and with SSR-FD, respectively.  $F_{\text{sup}}$  denotes the suppression ratio with and without SSR-FD processing in the allocated time range. Fig. 8 shows the  $F_{\text{sup}}$  histogram in all 66 patterns, where 78.5% of the patterns satisfy  $F_{\text{sup}} \leq$

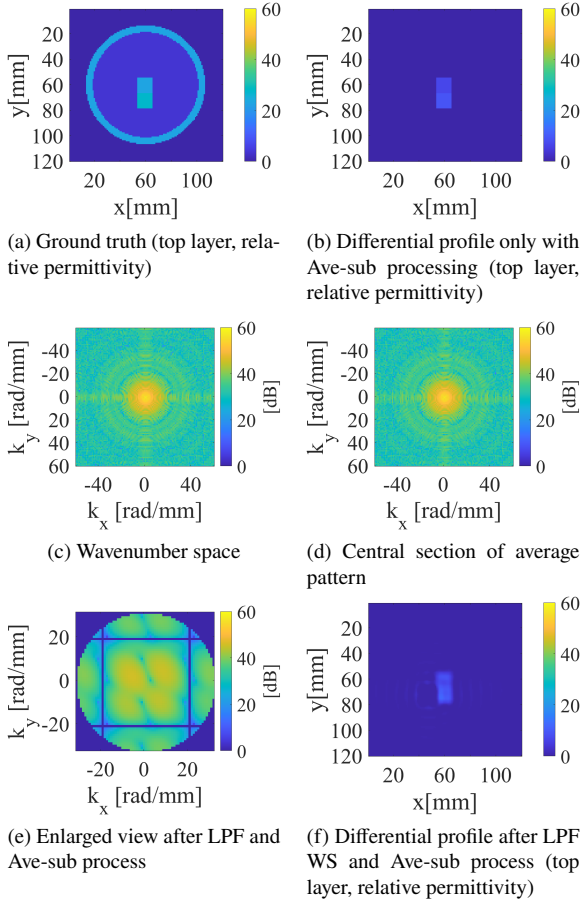


Fig. 9: Example of the WS compression and Ave-sub processing in the pattern #1.

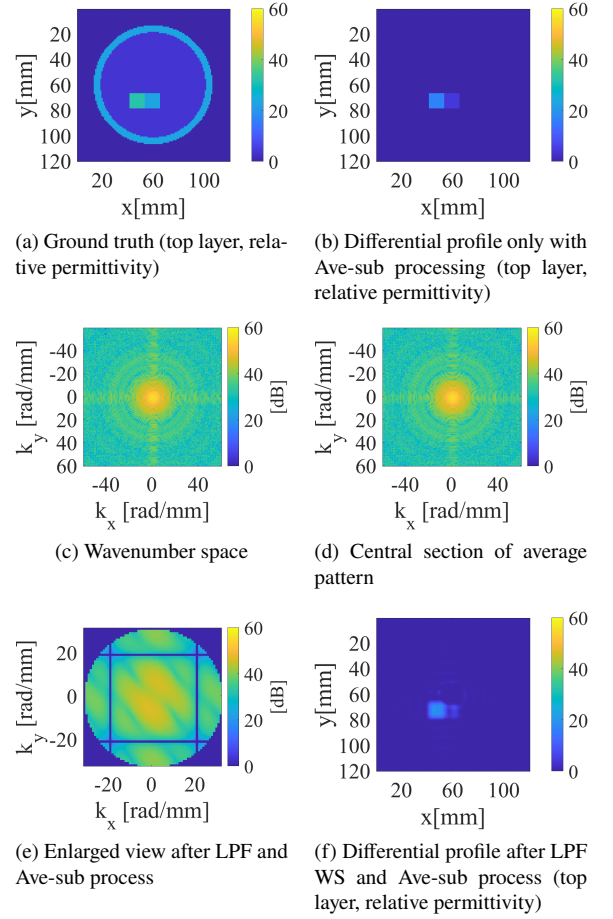


Fig. 10: Example of the WS compression and Ave-sub processing in the pattern #2.

0.1. This demonstrates the effectiveness of SSR-FD, which directly affects the quality of the post complex permittivity imaging.

### 3.2.2 WS Compression Data

WS compression examples are presented as follows. Fig. 9 and Fig. 10 show the results of WS LPF compression and Ave-Sub processing for the pattern #1 and #2, respectively. Here, the LPF parameter  $K_{\text{cutoff}}$  is set to 32 rad/m. As shown in these figures, differential profiles, as shown in Figs. 9-(b) and 10-(b), are almost recovered by the proposed dimension reduction scheme, which are also shown in Figs. 9-(f) and 10-(f). In particular, the dimension of CAE inputs and outputs is decreased from  $64^3 = 262144$  to  $32^3 = 32768$  using these processes. Notably, regarding the LPF parameters, we used  $K_{\text{cutoff}} = 16$  rad/m or 64 rad/m, to determine the appropriate  $K_{\text{cutoff}}$  value. Considering the balance between available spatial resolution and dimension reduction, as described in Sec. 2.3, we selected  $K_{\text{cutoff}} = 32$  rad/m in this case.

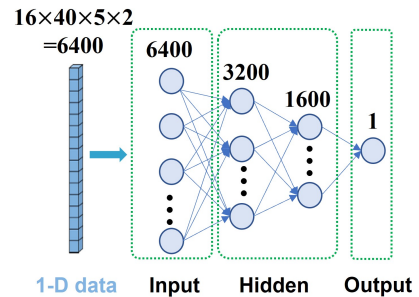


Fig. 11: The structure of the FC-MLP in the proposed method.

### 3.2.3 Reconstruction of Complex Permittivity

This section presents the 3D complex permittivity profile reconstruction results of the proposed scheme. Here, the proposed method uses five frequencies, namely, 3.0, 4.0, 5.0, 6.0, and 7.0 GHz, which are included in the effective bandwidth of the transmitted signal, and 16 combinations of the transmitters and receivers are used. In addition, the rotation

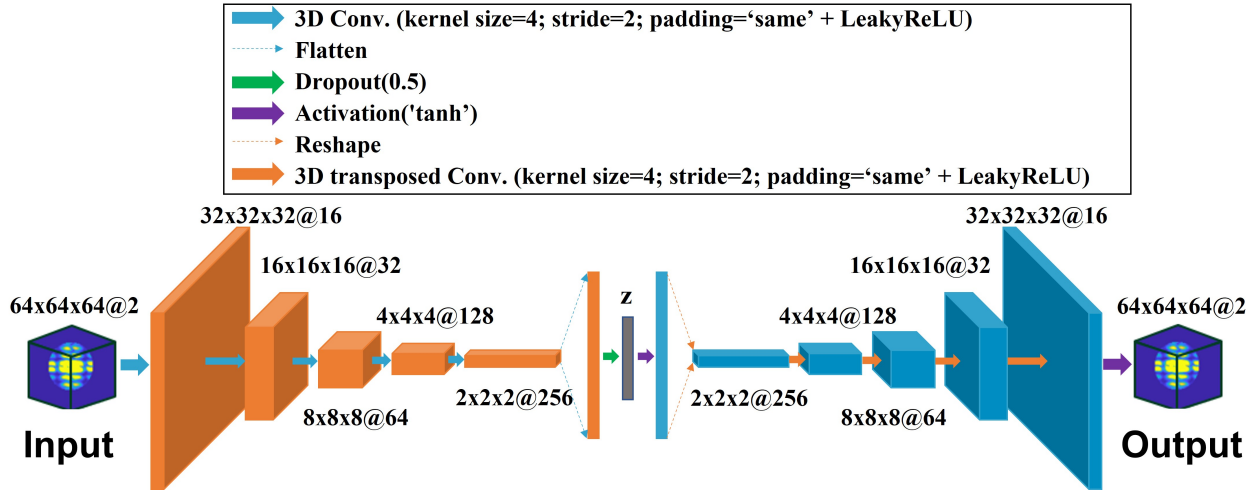


Fig. 12: Structure of 3D-CAE. The notation  $a \times b \times c @ d$  of each data box is defined as the number of pixels for Height ( $a$ ), Width ( $b$ ), Depth ( $c$ ), and Channel ( $d$ ), respectively.

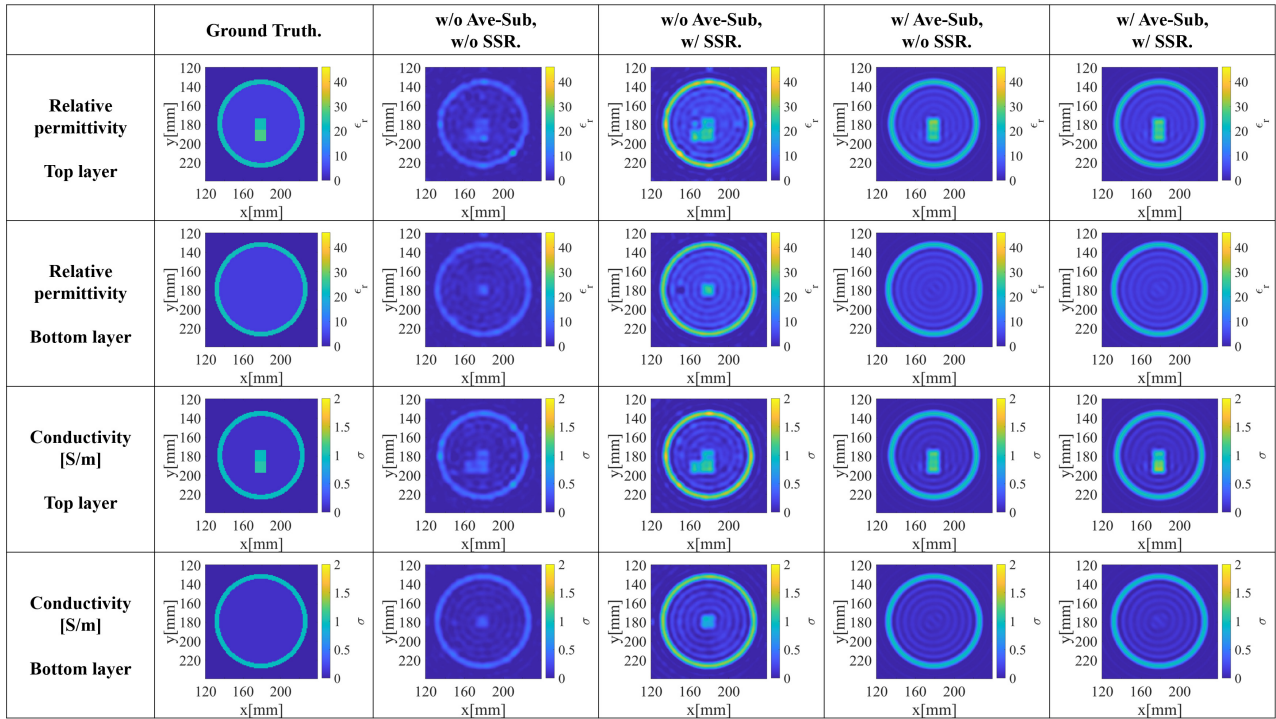


Fig. 13: Reconstruction results of relative permittivity and conductivity of pattern #1 with or without using the Ave-sub and SSR-FD processes. Color denotes each value of relative permittivity and conductivity of profile.

angle is varied within a range of  $0^\circ \leq \theta \leq 360^\circ$  with  $9^\circ$  intervals; that is, 40 samples along the  $\theta$  direction are used. Then, the real and imaginary parts of  $5 \times 16 \times 40$ -dimension data are separately input to the FC MLP. Fig. 11 shows the structure of the FC MLP, where batch normalization, dropout, and fully connected processes are applied between hidden layers. Figure 12 also shows the actual structure of the 3D-CAE model (described in Sec. 2.3), which was used in the proposed method. As shown in this figure, the kernel size of the convolution filter is set to 4, where the stride index is set to 2. To prevent over-fitting in the learning process, we

introduced several techniques, such as data normalization (minimum:0 maximum:1), dropout (rate=50 %), or hyper-parameter optimization (e.g., learning rate adjusted by the Adam (adaptive moment estimation) algorithm [21]). The activation function is set to Leaky RELU (Rectified Linear Unit), where the negative section allows a small gradient instead of being completely zero, helping to reduce the risk of overfitting in neural networks [22]. Numbers of epochs in the 3D-CAE and FC-MLP are 20000 and 320000, respectively, where the batch size are same as 65.

Here, the data set for the 66 phantom patterns is in-

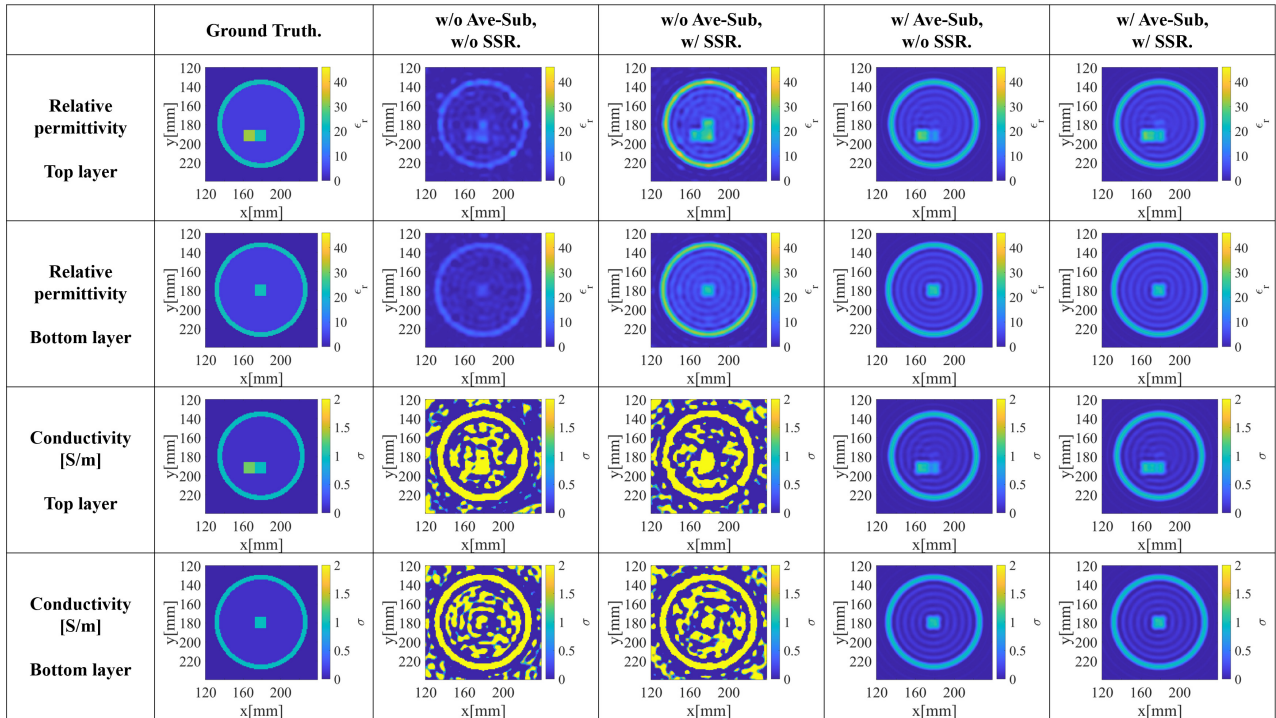


Fig. 14: Reconstruction results of relative permittivity and conductivity of pattern #2 with or without using the Ave-sub and SSR-FD processes. Color denotes each value of relative permittivity and conductivity of profile.

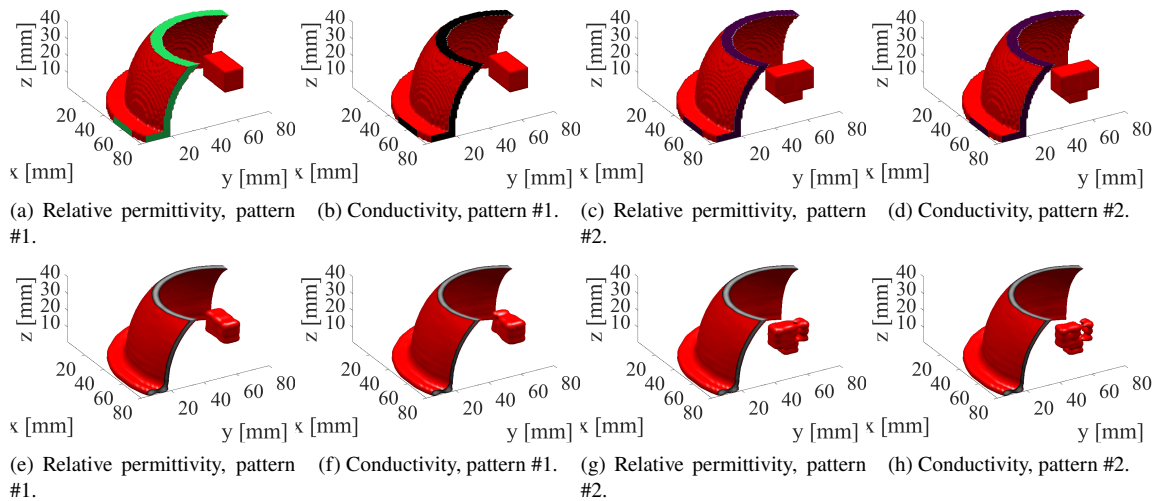
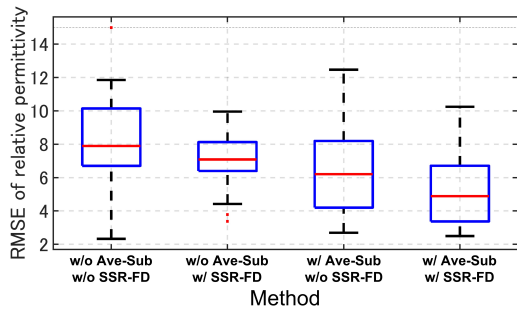


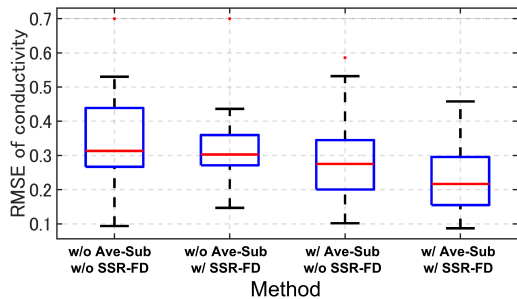
Fig. 15: The 3-D views of the reconstruction 3-D profiles in the patterns #1 and #2. The red isosurfaces represent the portion above the threshold of 20 for relative permittivity and 0.9 S/m for conductivity. 1st row : Ground truth profile. 2nd row: Reconstruction profile.

investigated using leave-one-out validation 66 times; in other words, 65 patterns are used for training data without any validation data for evaluating 1 test data. The 3D reconstruction result in terms of relative permittivity and conductivity for pattern #1 and #2 are shown in Figs. 13 and 14, respectively. The results obtained without SSR-FD and Ave-sub suffer from inaccuracy in providing almost the same profiles in both relative permittivity and conductivity. This is be-

cause the scattered data in FC MLP or the training data in the CAE dominantly include skin surface reflection or skin profiles. On the contrary, the reconstruction results obtained using both SSR-FD and Ave-sub show remarkably accurate profiles in both relative permittivity and conductivity. This is because the Ave-Sub processing can filter out the common patterns in the wave-number data, so only differential profiles are trained using the 3D CAE. SSR-FD processing also



(a) RMSE of relative permittivity



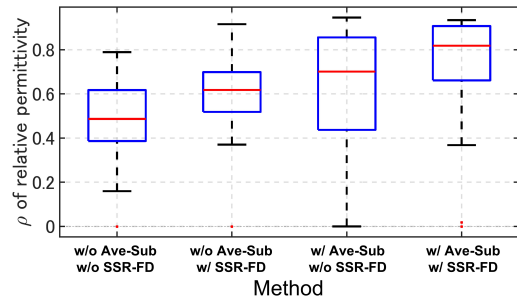
(b) RMSE of conductivity

Fig. 16: Box plots of RMSE of relative permittivity and conductivity in 66 different patterns. Red line is median value. Box denotes the interquartile range (IQR). Whisker denotes the most extreme data points but not considered outliers.

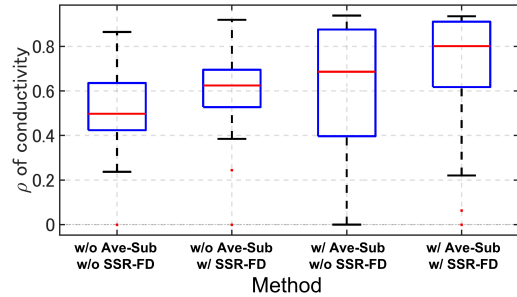
helps reconstruct the inner area of the phantom by eliminating the effect of skin surface reflection. In Fig. 14, it can be seen that the reconstructions without Ave-Sub processing suffers from many unnecessary responses. This is because the skin and some internal domains are dominant in the WS data without Ave-Sub processing, leading to overfitting. Fig. 15 also shows the 3D views of the reconstruction profiles in each case, where the reconstruction values are binarized using thresholds (20 for relative permittivity and 0.9 S/m for conductivity). This figure demonstrates that our proposed scheme successfully reconstructs the full 3D image without contaminated by any false images. Notably, the average computational times for Ave-Sub and 3D CAE processes for 20000 epochs are 12 seconds and 5 hours, respectively. The average computational times of SSR-FD and the FC MLP for 320000 epochs are 7 seconds and 20 minutes, respectively. The computational resources are as follows: Intel(R) Xeon(R) Gold 6330 CPU @ 2.00 GHz CPU, NVIDIA A100-PCIE-40GB and 1.00 TB RAM. After the above network is trained, 3D complex permittivity imaging can be performed using the scattering data in a few seconds.

### 3.2.4 Quantitative Error Analysis

Next, we introduce a quantitative error analysis using the root mean square error (RMSE) metric by comparing the ground truth and reconstruction profiles of relative permit-



(a)  $\rho$  of relative permittivity



(b)  $\rho$  of conductivity

Fig. 17: Box plots of Corrcoef of relative permittivity and conductivity in 66 different patterns. Red line is median value. Box denotes the interquartile range (IQR). Whisker denotes the most extreme data points but not considered outliers.

tivity and conductivity. which is defined as follows: Fig. 16 shows RMSE boxplots for the relative permittivity and conductivity under four different conditions, as in Fig. 13 and 14. As shown in Fig. 16, the proposed method (Ave-sub and SSR-FD processing) has the lowest median and interquartile range (IQR) in both of relative permittivity and conductivity, indicating its significant superiority. Furthermore, to test the reliability of these results, we illustrate boxplots of the correlation coefficients  $\rho$  obtained from comparing the ground truth and reconstruction profiles of the relative permittivity and conductivity shown in Fig. 17. As shown in Fig. 17, for both relative permittivity and conductivity, the median and IQR of the boxplot of  $\rho$  are the highest for proposed approach (Ave-sub and SSR-FD). Tables 2 and 3 summarize the median values of RMSE and  $\rho$ , respectively, as the representative statistical values. These tables show that the combination use of the Ave-sub and SSR-FD processes significantly improves the median RMSEs or  $\rho$  for both the relative permittivity and conductivity. The above error evaluations demonstrate that our method, specifically the combination of the Ave-sub and SSR-FD processes, exhibits significant advantages over other conditions regarding 3D complex permittivity imaging.

To demonstrate the superiority of the proposed scheme in terms of statistical significance, we calculate  $p$ -values through  $t$ -test. Table 4 and 5 summarizes the  $p$ -values for the RMSE and  $\rho$  results, respectively. In Table 4, all RMSE

Table 2: Median values of RMSEs for each condition for Ave-sub and SSR-FD processes.

Conditions	relative permittivity	conductivity
w/o Ave-Sub, w/o SSR-FD	7.90	0.313
w/o Ave-Sub, w/ SSR-FD	7.09	0.303
w/ Ave-Sub, w/o SSR-FD	6.21	0.275
w/o Ave-Sub, w/ SSR-FD	4.89	0.217

Table 3: Median values of  $\rho$  for each condition for Ave-sub and SSR-FD processes.

Conditions	relative permittivity	conductivity
w/o Ave-Sub, w/o SSR-FD	0.487	0.497
w/o Ave-Sub, w/ SSR-FD	0.618	0.625
w/ Ave-Sub, w/o SSR-FD	0.701	0.686
w/o Ave-Sub, w/ SSR-FD	0.819	0.801

$p$ -values between the condition with Ave-Sub and SSR-FD and the other conditions are less than 0.1. Moreover, all  $p$ -value of  $\rho$  between them are less than 0.01 (Table 5). These evaluations demonstrate the statistical superiority of the proposed imaging method with Ave-sub and SSR-FD.

### 3.3 Discussions

The results presented in Sec. 3.2 demonstrate that our scheme, *i.e.*, the 3D-WS-CAE, provides an accurate 3D complex permittivity profile, especially by combining Ave-sub and SSR-FD during pre-processing. While the previous study [17], demonstrated that scattered data could directly be converted into a complex permittivity profile, it did not present the full 3D image; instead, only 18 outputs for each discrete cubic cell were presented. In contrast, our scheme provides 3D images with a 1-mm voxel using the WS and 3D CAE-based dimension reduction scheme. In addition, as described in Sec. 1, deep-learning-based approaches for complex permittivity imaging [15, 16] require prior inputs, which are calculated or optimized using inverse scattering, resulting in a high computational cost. In contrast, our method does not require inverse scattering and can quickly provide the 3D complex permittivity profile once scattered data are obtained.

Nonetheless, since we could not always provide an accurate average breast model to the average subtraction process (Sec. 2.3) in the realistic scenario, certain errors can be generated in the reconstruction profile in the case of a realistic breast model. However, the proposed approach can provide an accurate initial estimate for a post inversion scheme, *e.g.*, CSI, to retain a physically reliable reconstruction and further

Table 4:  $p$ -value of RMSEs between the condition with Ave-sub and SSR-FD and other conditions in the proposed method.

Conditions	relative permittivity	conductivity
w/o Ave-Sub, w/o SSR-FD	$6.54 \times 10^{-2}$	$7.47 \times 10^{-2}$
w/ Ave-Sub, w/o SSR-FD	$3.70 \times 10^{-3}$	$4.90 \times 10^{-3}$
w/o Ave-Sub, w/ SSR-FD	$1.63 \times 10^{-9}$	$9.78 \times 10^{-2}$

Table 5:  $p$ -value of Corrcoeffs between the condition with Ave-sub and SSR-FD and other conditions in the proposed method.

Conditions	relative permittivity	conductivity
w/o Ave-Sub, w/o SSR-FD	$3.49 \times 10^{-13}$	$1.07 \times 10^{-9}$
w/ Ave-Sub, w/o SSR-FD	$3.40 \times 10^{-3}$	$5.70 \times 10^{-3}$
w/o Ave-Sub, w/ SSR-FD	$7.66 \times 10^{-6}$	$1.12 \times 10^{-4}$

improve a reconstruction accuracy, as introduced in [20].

## 4. Conclusion

This paper proposed a deep learning-based 3D complex permittivity reconstruction scheme that incorporating a 3D CAE and a FC MLP for microwave breast quantitative 3D imaging. Ave-Sub and WS compression are introduced as a preprocessing step of the 3D CAE to reduce the dimension of the input data in the post FC-MLP process. In addition, the SSR-FD scheme is used as a preprocessing step to extract distinct scattered responses from the inner area of the breast phantom. Experimental validations using an original simplified breast phantom with 18 replaceable cubes demonstrated that the proposed DNN scheme significantly improves the reconstruction accuracy of the 3D complex permittivity profiles.

## 5. Acknowledgment

This work was supported by JSPS KAKENHI Grant Number JP20H02161 and JST SPRING Grant Number JP-MJSP2131. The experimental tests have been greatly supported by Prof. Takamaro Kikkawa at Research Institute for Nanodevice and Bio System, Hiroshima University for providing the radar equipment.

## References

- [1] Sung, H, *et al.*, "Global Cancer Statistics 2020: GLOBOCAN estimates of incidence and mortality worldwide for 36 cancers in 185 countries", *CA Cancer J. Clin* 71, 209–249. <https://doi.org/10.3322/caac.21660> (2021).
- [2] E. Porter, H. Bahrami, *et al.*, "A wearable microwave antenna array for time-domain breast tumor screening", *IEEE Trans. Med. Imag.*,

- vol. 35, no. 6, pp. 1501-1509, Jun. 2016.
- [3] M. Sarafianou, A. W. Preece, *et al.*, "Evaluation of two approaches for breast surface measurement applied to a radar-based imaging system", *IEEE Trans. Antennas Propag.*, vol. 64, no. 2, pp. 609-617, Feb. 2015.
  - [4] T. Sugitani, S. Kubota, A. Toya, X. Xiao and T. Kikkawa, "A compact 4×4 planar UWB antenna array for 3-D breast cancer detection", *IEEE Antennas Wireless Propag. Lett.*, vol. 12, pp. 733-736, Oct. 2013.
  - [5] E. C. Fear, J. Bourqui, C. Curtis, *et al.*, "Microwave Breast Imaging With a Monostatic Radar-Based System: A Study of Application to Patients", *IEEE Trans. Microw. Theory Tech.*, vol. 61, no. 5, pp. 2119-2128, May 2013.
  - [6] Y. Chen, E. Gunawan, *et al.*, "Time of Arrival Data Fusion Method for Two-Dimensional Ultrawideband Breast Cancer Detection", *IEEE Trans. Antennas Propag.*, vol. 55, no. 10, pp. 2852-2865, Oct. 2007.
  - [7] J. Teo, *et al.*, "Breast Lesion Classification Using Ultrawideband Early Time Breast Lesion Response", *IEEE Trans. Antennas Propag.*, vol. 58, no. 8, pp. 2604-2613, Aug. 2010.
  - [8] M. T. Bevacqua, S. Di Meo, *et al.*, "Millimeter-Waves Breast Cancer Imaging via Inverse Scattering Techniques", *IEEE J. Electromagn. RF Microw. Med. Biol.*, vol. 5, no. 3, pp. 246-253, Sept. 2021.
  - [9] D. W. Winters, E. J. Bond, *et al.*, "Estimation of the Frequency-Dependent Average Dielectric Properties of Breast Tissue Using a Time-Domain Inverse Scattering Technique", *IEEE Trans. Antennas Propag.*, vol. 54, no. 11, pp. 3517-3528, Nov. 2006.
  - [10] T. Rubaek, P. M. Meaney, *et al.*, "Nonlinear Microwave Imaging for Breast-Cancer Screening Using Gauss-Newton's Method and the CGLS Inversion Algorithm", *IEEE Trans. Antennas Propag.*, vol. 55, no. 8, pp. 2320-2331, Aug. 2007.
  - [11] T. U. Gürbüz, B. Aslanyürek, A. Yapar, *et al.*, "A Nonlinear Microwave Breast Cancer Imaging Approach Through Realistic Body-Breast Modeling", *IEEE Trans. Antennas Propag.*, vol. 62, no. 5, pp. 2596-2605, May 2014.
  - [12] M. Lu, X. Xiao, Y. Pang, *et al.*, "Detection and Localization of Breast Cancer Using UWB Microwave Technology and CNN-LSTM Framework", *IEEE Trans. Microw. Theory Tech.*, vol. 70, no. 11, pp. 5085-5094, Nov. 2022.
  - [13] D. Alsaedi, A. Melnikov, K. Muzaffar, *et al.*, "A Microwave-Thermography Hybrid Technique for Breast Cancer Detection", *IEEE J. Electromagn. RF Microw. Med. Biol.*, vol. 6, no. 1, pp. 153-163, March 2022.
  - [14] J. Zhang, C. Li, W. Jiang, *et al.*, "Deep-Learning-Enabled Microwave-Induced Thermoacoustic Tomography Based on Sparse Data for Breast Cancer Detection", *IEEE Trans. Antennas Propag.*, vol. 70, no. 8, pp. 6336-6348, Aug. 2022.
  - [15] S. Costanzo, A. Flores and G. Buonanno, "Fast and Accurate CNN-Based Machine Learning Approach for Microwave Medical Imaging in Cancer Detection", *IEEE Access*, vol. 11, pp. 66063-66075, 2023.
  - [16] Khoshdel, Vahab, Mohammad Asefi, Ahmed Ashraf, and Joe LoVetri, "Full 3D Microwave Breast Imaging Using a Deep-Learning Technique", *J. Imaging*, 6, no. 8: 80, 2020.
  - [17] P. Zhu and S. Kidera, "Complex Permittivity Reconstruction Using Skin Surface Reflection and Neural Network for Microwave Breast Imaging", *IEEE J. Electromagn. RF Microw. Med. Biol.*, vol. 7, no. 4, pp. 425-431, Dec. 2023.
  - [18] K. Noritake and S. Kidera, "Boundary Extraction Enhanced Distorted Born Iterative Method for Microwave Mammography", *IEEE Antennas Wirel. Propag. Lett.*, vol. 18, no. 4, pp. 776-780, April 2019.
  - [19] Song, H., Sasada, S., Kadoya, T. *et al.*, "Detectability of Breast Tumor by a Hand-held Impulse-Radar Detector: Performance Evaluation and Pilot Clinical Study.", *Sci. Rep.*, Vol. 7, Nov. 2017.
  - [20] U. Hirose, P. Zhu and S. Kidera, "Deep Learning Enhanced Contrast Source Inversion for Microwave Breast Cancer Imaging Modality", *IEEE J. Electromagn. RF Microw. Med. Biol.*, vol. 6, no. 3, pp. 373-379, Sept. 2022.

- [21] K. Diederik and B. Jimmy, "Adam: A Method for Stochastic Optimization", *In International Conference on Learning Representations (ICLR)*, 2015.
- [22] A. L. Maas, A. Y. Hannun, A. Y. Ng, "Rectifier Nonlinearities Improve Neural Network Acoustic Models", 2014.



**Peixian Zhu** received the B.E. degree in automation engineering from the Shandong University of Technology, Zibo, China, in 2018, and received the M. E degree with the Graduate School of Informatics and Engineering, the University of Electro-Communications, Tokyo, Japan, in 2022. He is currently pursuing the D.E. degree with the Graduate School of Informatics and Engineering, University of Electro-Communications, Tokyo, Japan. He is also a next generation researcher (student) of Japan Science and Technology Agency (JST) from 2022 to 2025. His research interests include electromagnetic tomography as well as its applications.



**Shouhei Kidera** received his B.E. degree in Electrical and Electronic Engineering from Kyoto University in 2003 and M.I. and Ph.D. degrees in Informatics from Kyoto University, Kyoto, Japan, in 2005 and 2007, respectively. In 2009, he joined as an Assistant Professor with the University of Electro-Communications, Tokyo, Japan, where he is currently a full Professor with Graduate School of Informatics and Engineering in the University of Electro-Communications, Tokyo, Japan. His current research interest is in advanced radar signal processing or electromagnetic inverse scattering issue for ultra wideband (UWB) three-dimensional sensor or bio-medical applications. He has been stayed at the Cross-Disciplinary Electromagnetics Laboratory in the University of Wisconsin Madison as the visiting researcher in 2016. He has been a Principal Investigator of the PRESTO Program of Japan Science and Technology Agency (JST) from 2017 to 2021. He was a recipient of the 2012 Ando Incentive Prize for the Study of Electronics, 2013 Young Scientist's Prize by the Japanese Minister of Education, Culture, Sports, Science and Technology (MEXT), and 2014 Funai Achievement Award, 2022 KDDI Foundation Award, Contribution Award, and 2023 RIEC Award. He is a senior member of the Institute of Electrical and Electronics Engineers (IEEE), and the International Union of Radio Science (Union Radio-Scientifique Internationale, URSI), and a member of the Institute of Electrical Engineering of Japan (IEEJ), and the Japan Society of Applied Physics (JSAP).